

# Human Mars Entry, Descent, and Landing Architecture Study: Phase 3 Summary

Alicia Dwyer Cianciolo,<sup>1</sup> Ashley Korzun,<sup>2</sup> Karl Edquist,<sup>3</sup> Jamshid Samareh,<sup>4</sup>  
*NASA Langley Research Center, Hampton, VA 23681, U.S.A.*

Ron Sostaric<sup>5</sup>, Damien Calderon<sup>6</sup>  
*NASA Johnson Space Center, Houston, TX, 77058, U.S.A.*

Joseph A. Garcia<sup>7</sup>  
*NASA Ames Research Center, Mountain View, CA, 94035, U.S.A.*

**Over the past four years, NASA has directed the Entry, Descent and Landing Architecture Study (EDLAS) team to evaluate candidate technologies to deliver human-scale vehicles (carrying 20t payloads) to a precise location on the surface of Mars. The study, which initially considered four candidate vehicles, narrowed the design space to focus on two vehicles in Phase 3, one low and one mid lift-to-drag vehicle. Key design challenges exist for both, and the purpose of the Phase 3 analysis was to identify specific technology investment areas and opportunities to mature the vehicle designs beyond simulations to include ground and flight tests. This paper summarizes the detailed analyses performed on the two vehicle configurations, including aerodynamic and propulsive interference effects during the powered flight phase, vehicle packaging, as well as outer mold line and parametric mass model upgrades. The analyses were used to update models in the vehicle performance simulations. The simulation results showing the impact of the Phase 3 analyses on vehicle performance are also presented. Finally, a summary of the technology investment recommendations, including opportunities to validate models using wind tunnel tests and evaluate technologies at the moon, are presented. This paper offers a systems level overview of the more detailed analysis that will be presented in this special session.**

## I. Introduction

As NASA prepares to return humans to the moon, work continues within the Agency to characterize the entry, descent, and landing (EDL) vehicles and technologies needed to eventually land humans on Mars. Over the past four years, NASA has directed the Entry, Descent and Landing Architecture Study (EDLAS) to evaluate candidate technologies to deliver human scale vehicles (20t payloads) to the surface of Mars. Phase 1, performed in 2016, focused on developing Pre-Phase A EDL vehicle design concepts, parametric mass models, and integrated lander designs that could deliver a 20 t Mars Ascent Vehicle (MAV) [1]. Three vehicle concepts were developed that included two low lift-to-drag (L/D) deployable entry vehicles with a blunt forebody shape similar to past Mars robotic missions and one rigid mid-L/D vehicle similar to but smaller than the one assumed in the Design Reference Architecture 5 (DRA5) [2]. Results of the Phase 1 study indicated that all three concepts satisfied the mission assumptions outlined by the

---

<sup>1</sup> Aerospace Engineer, Atmospheric Flight and Entry Systems Branch, AIAA Senior Member.

<sup>2</sup> Research Aerospace Engineer, Atmospheric Flight and Entry Systems Branch, AIAA Member.

<sup>3</sup> Aerospace Engineer, Atmospheric Flight and Entry Systems Branch, AIAA Associate Fellow.

<sup>4</sup> Aerospace Engineer, Vehicle Analysis Branch (E401), AIAA Associate Fellow.


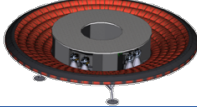
<sup>5</sup> Safe and Precise Landing Integrated Capabilities Evolution Project Manager, AIAA Senior Member.

<sup>6</sup> Aerospace Engineer, Structures Branch, AIAA Member.

<sup>7</sup> Aerospace Engineer, Systems Analysis Office, Aeronautics Directorate, AIAA Senior Member.

Evolvable Mars Campaign (EMC) [3]. Therefore, Phase 2, performed in 2017, expanded the EDL vehicle integration evaluation of single MAV payload to now include packaging of the remaining elements of the notional human Mars surface mission manifest [4]. In Phase 2, a fourth vehicle was also added for analysis, a rigid low-L/D capsule. Extensive packaging and three degree-of-freedom (DOF) trajectory analyses were performed to determine the landing accuracy, propellant consumption, and guidance requirements of the four vehicles. Key technology gaps were identified in the areas of supersonic retropropulsion (powered descent), entry guidance, powered descent guidance, and navigation. The Phase 2 study found that the capsule concept did not satisfy the EMC packaging constraints and, due to the vehicle's large ballistic coefficient, also required twice as much propellant to land the same 20 t payload as the other three concepts. Therefore, the capsule concept was removed from future analysis. Additionally, it was also noted that the two deployable low-L/D concepts offered similar flight performance capability at the Pre-Phase A level. It was therefore decided to perform the next level of analysis in Phase 3 using only one deployable concept. EDLAS Phase 3 continued to increase the fidelity of analysis to identify technology gaps using one mid-L/D and one low-L/D vehicle. The entry concepts for Phase 3 are shown in Table 1.

**Table 1. EDLAS Phase 3 EDL Vehicle Summary**

Name	Shape	Vehicle Dimensions	Launch Mass	Entry Mass	Ballistic Coefficient	L/D
Mid-L/D		22m (l) x 7.3m (h) x 8.8m (w)	66t	62t	380 kg/m <sup>2</sup>	0.55
Low-L/D		4.3m (h) x 16m diameter	57t	49t	155 kg/m <sup>2</sup>	0.15

Key design and technology challenges remain for both vehicles. The purpose of Phase 3, conducted in 2018 and 2019, was to (1) address specific technology gaps identified in Phase 2 using modeling and simulation and (2) to identify investment areas and opportunities to mature the vehicle designs in future ground and flight tests. The following sections of the paper summarize the detailed analysis performed on the two vehicle configurations, the results of the analysis and recommended technology investments. Additionally, opportunities to validate models using wind tunnel tests and to evaluate integrated vehicle designs using ground and flight test are also described. Section II summarizes the Phase 3 effort to characterize aerodynamic interference during the powered flight phase. Section III presents the Phase 3 payload packaging work performed for the mid-L/D vehicle as well as outer mold line and parametric mass model upgrades. These aerodynamic and vehicle model updates are incorporated in the trajectory performance simulation. Therefore, Section IV shows the simulation results and discusses the impacts of the aerodynamic-propulsive interference on both vehicles. Finally, as NASA prepares to send humans to the Moon, a summary of the specific aspects of Mars human-scale EDL that can be demonstrated in the lunar environment is presented. This paper offers a systems-level overview of the more detailed analyses that will be presented in this special session.

## II. Aerodynamic-Propulsive Interference Effects During Powered Descent

Until EDLAS conducted higher fidelity vehicle analysis in Phase 2, the general performance simulation assumption was that, after descent engine initiation, thrust was the dominant force on the vehicle, and therefore, all aerodynamic forces and moments on the vehicle during this phase of flight were set equal to zero. For vehicles where the total aerodynamic surface area is small compared to the engine exit area, such as is typical for the recovery of launch vehicles, this is a reasonable assumption. However, for large, human-scale landers, like those considered here, that utilize a large aerodynamic surface area to decelerate in the Martian atmosphere and control attitude, this assumption is not conservative. In fact, depending on the engine configuration, aerodynamic axial force equivalent to the thrust of a single engine or more can be produced after engine initiation as the vehicle decelerates through supersonic to transonic speeds. Knowledge about the flowfield and vehicle stability during this phase of flight, which affects the design of other subsystems including the reaction control system and navigation sensors, remains an active area of research and development. Therefore, a key task of EDLAS Phase 3 was to develop an aerodynamic interference model based on computational fluid dynamics (CFD) analysis of the powered descent phase using expected flight conditions generated in the performance simulation. The following subsections summarize the

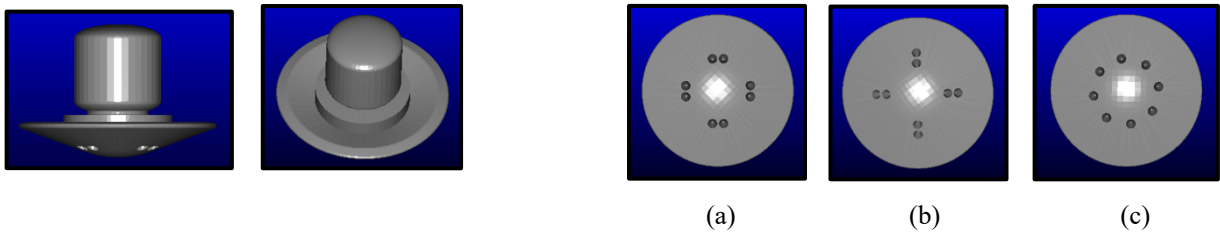
approach used to generate the aerodynamic interference model, the models developed for each vehicle, and the plan for validating the CFD through ground testing. A detailed description of the analysis and results can be found in [5].

### A. Model Development Approach

The development of powered descent aerodynamic interference models for each vehicle is entirely computational in this study, as limited relevant ground test data exists for empirical model development, and the inability to simulate flight environments and operation will result in a reliance on computational tools to generate aerodynamics models for an eventual flight implementation. To define the geometries, engine configurations and orientations (e.g., cant angle, scarfed nozzles, etc.) are identified from prior mechanical integration and structural analyses. Figures 1 and 2 show the engine configurations studied for the mid-L/D and low-L/D vehicles, respectively. Each vehicle assumes eight, liquid oxygen and methane ( $\text{LO}_2/\text{CH}_4$ ), gas generator cycle engines. The low-L/D vehicle uses 100 kN engines, and the mid-L/D vehicle uses 120 kN engines in this analysis. Only one engine configuration was considered for the mid-L/D vehicle due to vehicle constraints on accommodation and integration. The length of the mid-L/D vehicle (without flaps) is 19.8m. To simplify the CFD grid generation, and because there are multiple design options for exposing the engines after completion of the hypersonic phase of flight, the vehicle assumes a smooth geometry with no cavities. As such, the nozzles are scarfed, spaced 1.5 m apart, and canted outboard  $10^\circ$  to closely follow the vehicle OML. For the low-L/D vehicle, the forebody (heatshield) diameter (16.4m) and aftbody shape (of a notional habitat payload) are smooth and simplified for grid generation and because the forebody environments dominate aftbody environments during the early portions of powered descent. Similar to the mid-L/D engine integration, there are no cavities around the engines, and the low-L/D nozzles are scarfed and canted outboard  $5^\circ$ . Three engine configurations are considered. The baseline, named “Doublet-A” uses four pairs of engines, spaced  $90^\circ$  apart near the outboard limit of the 9.1 m diameter rigid center body is shown in Fig. 2a. A second configuration, “Doublet-B”, assumes the engines are also in pairs but aligned radially from the center body. See Fig. 2b. Finally, a third engine configuration places all eight engines evenly spaced about the rigid center body, 3.45 m radially outboard from the nose is shown in Fig. 2c.



**Fig. 1 Mid-L/D engine configuration evaluated for aerodynamic interference effects.**



**Fig. 2 Low-L/D vehicle configuration considered for aerodynamic interference effects (left); Baseline engine configuration a) (Doublet-A), b) Doublet-B, and c) symmetric engine spacing (right).**

Four CFD tools, each with prior experience simulating powered descent at various scales and conditions, are applied across the geometries shown in Figs. 1 and 2: Fully Unstructured Navier-Stokes Three Dimensional (FUN3D) [6], LociCHEM [7], Data Parallel Line Relaxation (DPLR) [8], and OVERset gridFLOW solver (OVERFLOW) [9]. The run matrix considered the vehicle flight conditions from supersonic engine initiation through transonic and subsonic conditions. Tables 2 and 3 show the freestream conditions simulated for the mid-L/D and low-L/D vehicles, respectively. The angle of attack is fixed at  $0^\circ$  for the low-L/D vehicle and  $90^\circ$  for the mid-L/D vehicle, and the maximum throttle setting is 80%. Conditions at engine initiation differ for the mid-L/D and low-L/D vehicles with performance results indicating that engine initiation for the low-L/D vehicle may occur near Mach 2.4, while the mid-L/D initiation starts closer to Mach 2.1, as a result of the higher available thrust for the mid-L/D vehicle in this analysis. A detailed discussion of the CFD analysis is provided in [5].

**Table 2. Mid-L/D CFD Test matrix (90 deg angle of attack)**

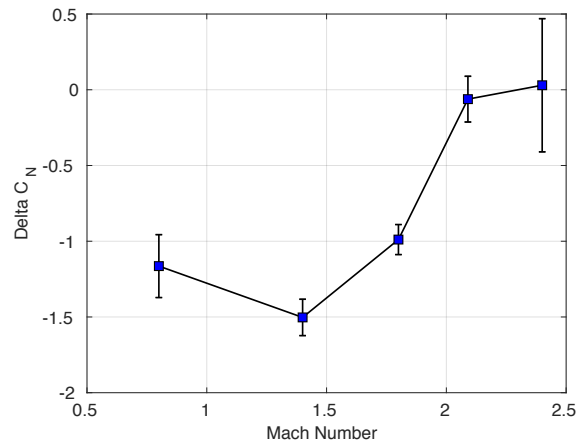
Case	$M_\infty$	$V_\infty$ (m/s)	$T_\infty$ (K)	$p_\infty$ (Pa)	$q_\infty$ (Pa)	$\rho_\infty$ (kg/m <sup>3</sup> )
1	2.09	492.27	225.02	417.22	1210.02	0.0098
2	1.80	424.82	225.60	430.13	930.50	0.0101
3	1.40	329.44	226.30	446.00	583.57	0.0104
4	0.80	186.92	227.45	473.30	203.94	0.0110
5	2.40	559.28	212.84	387.77	1508.04	0.0096

**Table 3. Low-L/D CFD Test Matrix (0 deg angle of attack)**

Case	$M_\infty$	$V_\infty$ (m/s)	$T_\infty$ (K)	$p_\infty$ (Pa)	$q_\infty$ (Pa)	$\rho_\infty$ (kg/m <sup>3</sup> )
1	2.52	587.63	216.19	273.37	1155.67	0.0067
2	2.40	560.60	216.53	284.73	1093.82	0.0070
3	2.00	469.03	217.53	324.63	869.15	0.0079
4	1.40	329.36	218.63	386.48	507.85	0.0094
5	0.80	189.10	219.50	442.92	191.16	0.0107
6	2.78	642.78	214.95	235.35	1212.83	0.0058

**B. Aerodynamic Interference Model Summary**

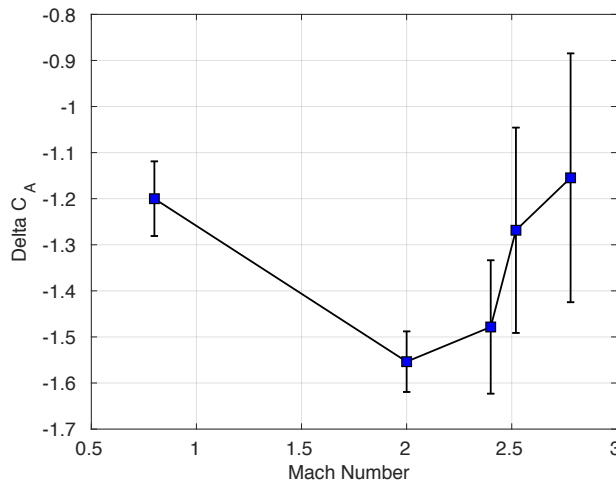
A total of 77 CFD solutions were completed for both vehicles including powered (engines on) and unpowered (engines off) cases [5]. The output yielded 6-component forces and moments for the powered and unpowered configurations in order to quantify the change in (e.g., delta) in aerodynamics due to the engines plume interactions, defined as the difference between the unpowered and powered aerodynamics. Figure 3 shows the difference in normal force coefficient (Delta  $C_N$  = Powered  $C_N$  – Unpowered  $C_N$ ) over the trajectory (decelerating from right to left) as the vehicle slows down from supersonic to subsonic speeds. A value of zero in Fig. 3 indicates that there is no reduction in  $C_N$  when the engines are on. The error bars represent  $\pm 3\sigma$  variations in the underlying data due to unsteadiness in individual solutions and code-to-code differences. The data in Fig. 3 is then applied in the flight mechanics simulation to account for aerodynamic interference, providing a more representative model of the forces on the vehicle during powered flight. Results are shown in Section IV. See [5] for a detailed discussion of the physics producing the trend shown in Fig. 3.



**Fig. 3 Difference in normal force coefficient (powered – unpowered) during the supersonic-to-subsonic portion of the powered descent phase for the mid-L/D vehicle.**

Similarly, Fig. 4 shows the difference in axial force coefficient for the low-L/D vehicle. Because the vehicle flies with a different orientation, with an angle of attack near zero, axial force, not normal force, is most affected in powered flight. As with the mid-L/D model, the error bars represent  $\pm 3\sigma$  variations in the underlying data due to unsteadiness in individual solutions and code-to-code variations, and uncertainties are smaller for conditions with significant inboard plume interference (at lower Mach numbers). The present model assumes the uncertainties bound the amplitude, but not frequency, of oscillations in force and moments coefficients. Additionally, all other forces and moments are nominally zero for the low-L/D vehicle, as these trends have been shown to hold over small angles of attack [10,11]. These results are implemented into the performance simulation, described in the section IV, to evaluate the effect on parameters like descent timeline, propellant consumption, and vehicle stability. A complete summary of the CFD analysis and results performed for EDLAS Phase 3 can be found in [5].

It is important to note that none of the CFD analyses used to generate the aerodynamics interference models have been validated, as relevant data from either ground testing or flight testing does not presently exist. Efforts to generate such data are underway, with an upcoming wind tunnel test campaign described below. It is also noted the computational cost associated with each one of the 77 solutions generated to develop these rudimentary models required several hundred thousand CPU hours, with considerable concessions on spatial resolution and modeling fidelity. Efforts to implement the FUN3D CFD code to run on Graphical Processing Units (GPUs) was the focus of a 2019 feasibility study performed under competitive research awards from Oak Ridge National Laboratory's Leadership Class Computing Facility. Results of this work, which use the low-L/D baseline vehicle as the application, can be found in Ref [12]. Under the Oak Ridge effort, it has been demonstrated that powered descent aerodynamics solutions with 1-2 orders of magnitude greater spatial resolution and with higher fidelity modeling approaches can be generated in days, not years. To fully utilize gains in computational efficiency, however, relevant validation data from ground testing and flight testing must be realized.



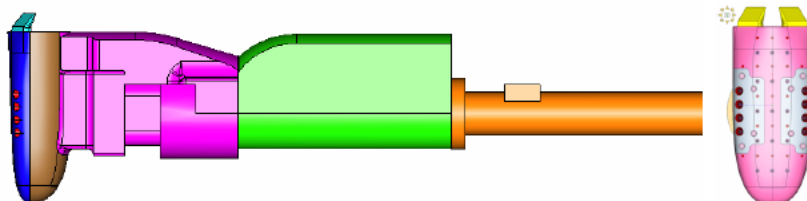
**Fig. 4 Difference in axial force coefficient (powered – unpowered) for the low-L/D vehicle during the supersonic-to-subsonic portion of powered descent.**

### C. Wind Tunnel Tests

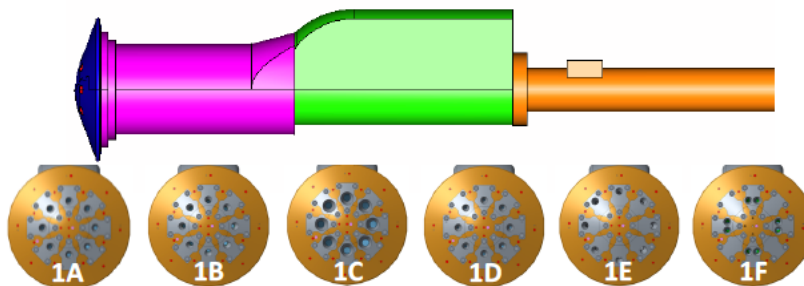
Wind tunnel testing, flight testing, and computational fluid dynamics (CFD) analysis all will play a critical role in advancing the atmospheric powered descent technology. Ultimately, a flight test will be needed to reduce risk for any human scale Mars entry vehicle. However, a near term opportunity to partner with NASA's Aerosciences Evaluation and Test Capability Program (AETC) is available. AETC adopted CFD evaluation as a capability challenge in 2018. The challenge seeks to determine if CFD can reliably predict challenging EDL aerosciences problems in the Mach 2.4 to 4.6 range, which matches the NASA Langley Unitary Plan Wind Tunnel high-speed section Mach number range. AETC was looking for complex vehicle shapes and configurations to support the task. Therefore, the low and mid-L/D vehicle powered flight configurations were offered as candidates for the challenge. The primary limitation to participating in the challenge is that the vehicles would be evaluated for wind-tunnel environment rather than flight environment. Consequently, new CFD cases have to be run. Additionally, due to the limited size of the tunnel test section, scaling the vehicles engines to achieve similar powered flight conditions is a challenge. While it is not possible

to match some of the relevant scaling parameters compared to flight conditions, a test matrix will be executed to provide valuable information regarding aero/propulsion interactions that exist during supersonic powered descent.

Wind tunnel tests of powered flight are planned in 2020 for both the low and mid-L/D vehicles. The mid-L/D vehicle will consider a single engine configuration, while the low-L/D will consider several configurations using removable plugs in a single test article, each nozzle insert having a different exit area, area ratio, cant angle, or location on the heatshield. Figures 5 and 6 show the model configurations for the mid and low-L/D vehicles respectively. High pressure air will be sent through the sting and out the engine nozzles in each model. A parametric investigation of supersonic retropropulsion on subscale versions of the human-scale Mars powered descent vehicles is planned. Table 4 provides a summary of the low-L/D test matrix parameters. The tests data will include aerodynamic forces and moments that will be compared with CFD runs in the tunnel environment. Details of the model design and pre-test CFD can be found in Ref [13].



**Fig. 5 Mid-L/D wind tunnel model and sting.**



**Fig. 6 Low-L/D wind tunnel model and sting, with variations in engine location.**

**Table 4. Low-L/D tunnel planned test matrix.**

Independent parameter	Number of values	Range of values or discrete values
Model Configuration	7	1, 1A, 1B, 1C, 1D, 1E, 1F
Mach number	3	2.4, 3.5, 4.6
Angle of attack (deg)	TBD	Approx. -10 to +20 deg, every TBD deg
HPA pressure (psia)	TBD	TBD
Roll angle (deg)	2	0 and 22.5 or 45

An additional wind tunnel test will be conducted on the mid-L/D vehicle to determine the effect of the control surfaces (body flaps) at various conditions during unpowered flight. Various aileron and elevon combinations will be tested by swapping out body flaps that are configured at different angles relative to the slender body. These configurations will be evaluated for a range of Mach between 2.4 and 4.6 as well as angles of attack from 40 to 70 degrees and side slip angles up to 10 degrees. As mentioned, the wind tunnel conditions won't match the Mars flight conditions exactly, but CFD analysis of the model in the tunnel will provide direct comparison with tunnel data for validation purposes. Despite the flight and wind tunnel test differences, lessons learned regarding how well CFD is able to predict the flow around the control surfaces will be used to assess how well the process can be used for future test flights and eventually Mars missions. The test is scheduled for mid-January 2020. Detailed information about the planned test and specific tunnel CFD runs for both vehicles are planned for publication in the AIAA Aviation conference in 2020. In 2021, there are plans for a special session at the AIAA SciTech conference that will include detailed papers of both the experimental and CFD results of these test including a focus on modeling of the empty tunnel to help characterize the flow field upstream of the test section for these wind tunnel models.



### III. Mid-L/D Vehicle Upgrades

The mid-L/D had several design challenges that were addressed in EDLAS Phase 3. First, the initial design of the outer mold line included simplified body flaps with a sharp transition off the body onto the flaps which would result in flow separation and high temperatures during hypersonic flight. Work was performed to modify the vehicle shape to eliminate the transition. Additional analyses were performed to consider the impact of shortening the total vehicle length, not only to take advantage of mass savings, but also to accommodate the SLS short fairing options. To date, payload packaging efforts have considered only vertical arrangements of the surface elements in the entry vehicles. The 2018 Mars architecture studies yielded an updated three-lander payload manifest, notably transitioning from a monolithic (single large) habitat structure to a modular design (multiple smaller compartments). Therefore, a packaging effort was performed to evaluate how the new manifest could be arranged in both the full size and shorter version of the mid-L/D vehicle and to verify that center of gravity location requirements for flight were satisfied. Finally, as architecture considerations change, especially with NASA's pivot to the moon, work to update and expand parametric mass modeling of individual elements of the mid-L/D took place in EDLAS Phase 3. Details of these updates are summarized in this section.

#### A. Outer Mold Line Updates

During EDLAS Phase 3, efforts were made to update the outer mold line of the mid-L/D vehicle to improve the transition on the windside aftbody onto the body flap as well as to design more realistic body flaps that could be controlled with a linear actuation system similar to that used in the NASA's Space Shuttle. Figure 7 shows the Phase 2 vehicle design [14,15] and Fig. 8 shows the modifications for the Phase 3 vehicle design. Based on this new vehicle configuration, structural sizing and hypersonic aerodynamics models were updated. This updated Phase 3 configuration is also the baseline shape for the supersonic windtunnel testing mentioned in section II c above. A more detailed summary of the vehicle sizing and outer mold line updates are found in Ref [16].

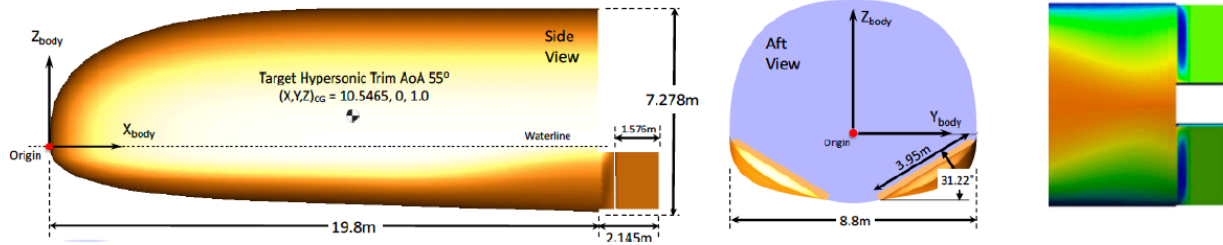


Fig. 7 CobraMRV 2908b Phase 2 configuration.

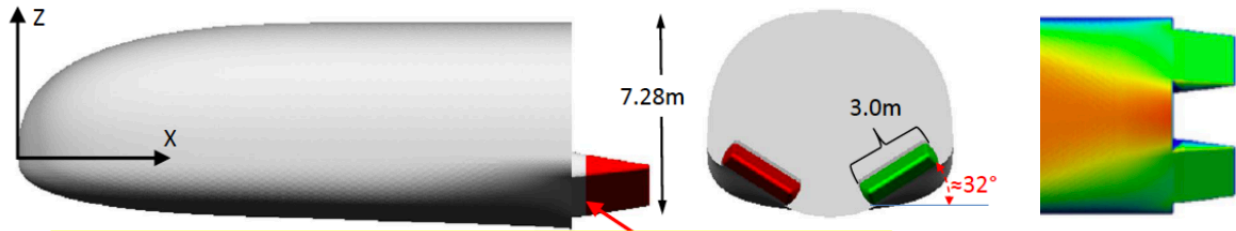
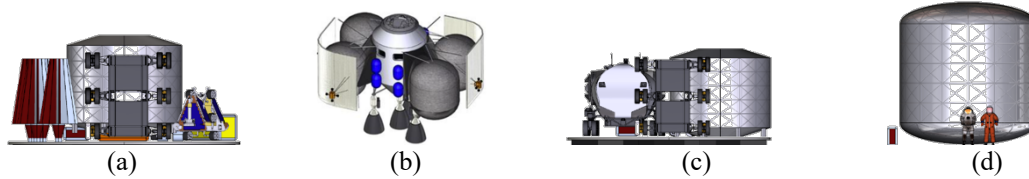


Fig. 8 CobraMRV 2908g Phase 3 configuration

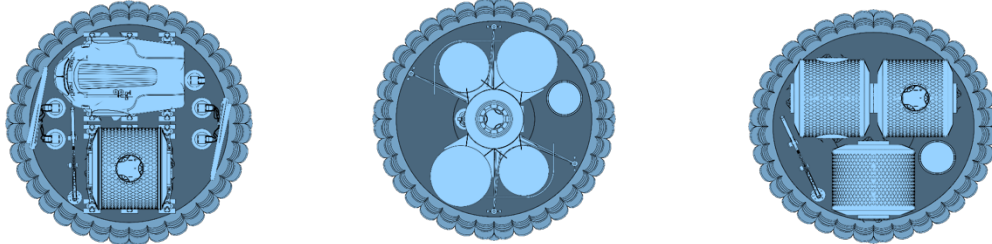
#### B. Packaging and Structures

EDLAS Phase 1 and 2 assumed a notional surface manifest shown in Fig. 9 that included four 20 t payload landers. The first lander included a fission surface power, 100 km-class mobility rovers and associated logistics and supplies (Fig. 9a). The second lander contains the Mars Ascent Vehicle (MAV) (Fig. 9b) and an atmospheric In-Situ Resource Utilization (ISRU) system to generate MAV propellant. The third delivers a pressurized rover, mobility rover and logistics container (Fig. 9c). The fourth lander, which delivers the crew, is the surface habitat (Fig. 9d). However, the 2018 Mars architecture studies yielded an updated three-lander 22 t payload manifest, notably transitioning from a monolithic (single large) habitat structure to a modular design (multiple smaller compartments). The three-lander payload is shown for the vertical packaging configuration in Fig. 10. The first lander includes five kilowatt units, electrical cabling and a power distribution box. The lander also delivers a hoist, pressurized rover, mobility chassis, crew support rover, and the initial habitation module. The second lander, similar to the Phase 2 second lander, delivers

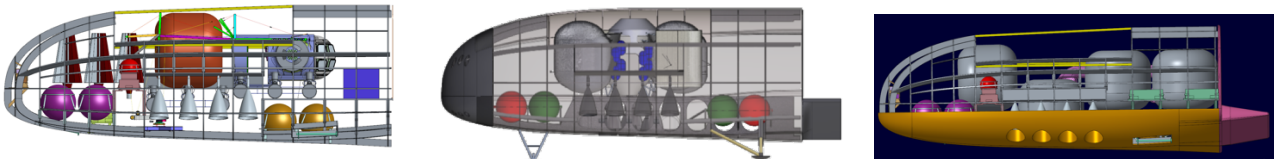
the MAV and ISRU unit. The third lander deliver a crew of four, an airlock, two habitable logistics modules, a second hoist, science equipment and surface suits. Therefore, a packaging effort was performed to evaluate how the new manifest could be arranged in both the full size and shorter version of the mid-L/D vehicle and verify that center of gravity location requirements for flight were satisfied. Figure 10 shows the updated vertical packaging arrangement. Figure 11 shows the new lander manifest packaged in the mid-L/D vehicle. A full description of the packaging effort is found in Ref [16]. The effort verified that the payload elements fit within the available volume and the packaged center of gravity meets the requirements for stable flight. However, the individual payload elements were not resized to handle the difference directions of the launch (aeroshell axial loads, payload lateral loads) and entry loads (aeroshell lateral loads, payload axial loads).



**Fig. 9 EDLAS Phase 2 lander payloads: Lander 1: power, unpressurized rover, cargo offloading, science payloads logistics module; (b) Lander 2: MAV, ISRU, access tunnel; (c) Lander 3: Pressurized rover, logistics module, surface mobility; (d) Lander 4: Habitat.**



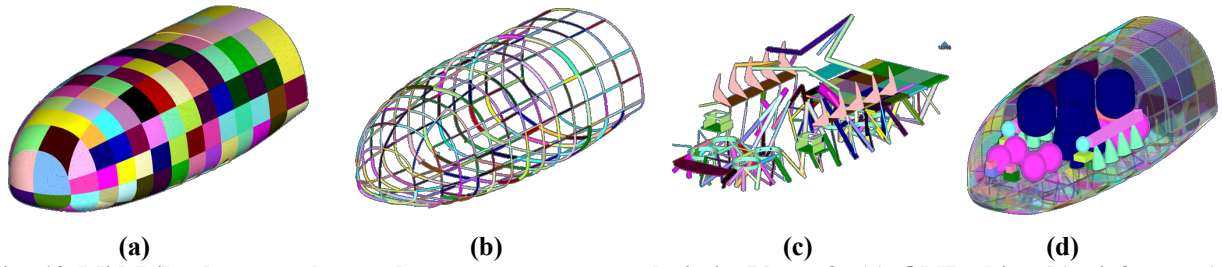
**Fig. 10 EDLAS Phase 3 lander elements looking down on the vertical packaging arrangement: lander 1, includes a pressurized rover, fission power, surface mobility system, logistics/habitat container; Lander 2, Mars Ascent vehicle**



**Fig. 11 Three lander configurations packaged in the mid-L/D vehicle.**

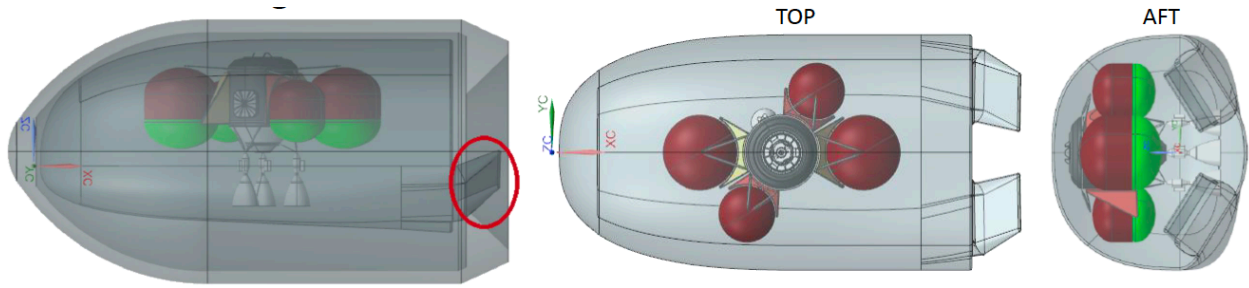
In addition to the outer mold line updates and packaging work, the Phase 3 effort included the reevaluation of the mid-L/D structural and thermal protection system (TPS) sizing in order to update the mass estimate of the entry vehicle. The study assumed the 22t payload and the structure was sized assuming Aluminum 2024 construction. A bay floor door was added for operation during the powered descent phase and MAV support struts were added for dynamic stability. Figure 12 shows the OML skin, airframe, substructure and cargo elements that were resized during the study. The structures were designed to accommodate a 5 g axial load, a  $\pm 2$  g lateral load and a 3 g Mars landing load. A full description can be found in [16]. In addition, to the updated structural mass, engineering level aerothermal analysis was performed to update the vehicle Thermal Protection System for the updated OML. For all the changes made to the mid-L/D vehicle, the major factor in the overall increased entry vehicle mass (structure + TPS) was due to increased payload mass. The total structural mass increased from 8.5t in 2017 to 10.3 t in 2019.





**Fig. 12 Mid-L/D elements that underwent structure analysis in Phase 3. (a) OML skin, (b) airframe, (c) substructure and (d) with the cargo elements and tanks.**

An additional study considered the feasibility of packaging the payload in the SLS 10 m diameter short fairing (19.1 m tall). Figure 12 shows that the initial packaging of the largest element, the MAV, fits in the available volume. It is noted that the body flap (circled in the left of Fig. 13) may have to be completely stowed in order to meet the SLS length requirements. It remains to be determined if the reduced volume can accommodate additional decent propellant tanks and maintain center of gravity limitations. A further summary of the packaging and TPS update can be found in Ref [16,17]

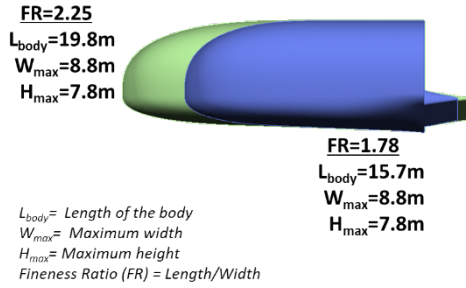


**Fig. 13 Mid-L/D packaging of the MAV in the SLS 10 m diameter short fairing.**

### C. Vehicle Closure

Preliminary closure results for the shortened mid-L/D (fineness ratio (FR) =1.78) compared to the baseline (FR=2.25) OML were performed using the Co-Optimization Blunt-body Re-entry Analysis (COBRA) multidisciplinary design analysis and optimization (MDAO) process [18, 19] for a 20t payload. In this closure analysis the aerodynamics and aerothermodynamics are obtained from the Configuration Based Aerothermal (CBAERO) engineering level tool. The vehicle trajectories are simulated in 3DOF using the Program to Optimize Simulated Trajectories (POST2) tool and Thermal Protection System (TPS) is optimized and sized using the TPSSizer tool. Finally, the other subsystem masses are obtained based on various Mass estimation relationships (MERs) and the process provides the option for a fallout arrival mass at the end of a closure iteration and is repeated until a target payload convergence is achieved. One advantage to this streamline MDA approach is that the assessment of various vehicles can be obtained using consistent assumptions, tools, and constraints. In this case, the same entry conditions and down range constraints are imposed on the trajectory analysis, and a target power descent thrust of 100 kN per engine is used. The converged results are shown in Table 5, below. Key results show that the shorter vehicle successfully lands the 20t payload and meets the downrange constraint of 1,275km such that the power descent staging conditions occurs at a lower altitude, lower flight path angle (FPA), and higher Mach number. The largest mass reduction is seen in the vehicle structure mass attributed to the lower surface area and similar peak dynamic pressure. However, the TPS mass increases slightly which is attributed to the higher heating associated with the higher ballistic coefficient due to the reduced surface area. This leads to a reduction of ~4,000kg (~4t) in the arrival mass which translates into approximately 1,000kg (1t) reduction in the arrival mass for every meter reduction in vehicle body length.

**Table 5. Shorten Mid L/D Vehicle Closure Results**



20t Payload, 100kN Target Engine Size			
	units	FR=2.25	FR=1.78
Down Range	km	1,275	1,275
Power Descent Stage FPA ( $x_{max12}$ )	deg	-10.6	-5.1
Power Descent Stage Mach ( $x_{max10}$ )		1.9	2.3
Power Descent Stage Altitude ( $x_{max11}$ )	m	3,558	3,000
Peak Dynamic Pressure	Pa	8,832	9,129
<b>Total Vehicle Structure Mass</b>	<b>kg</b>	<b>12,168</b>	<b>8,796</b>
<b>Total TPS Mass</b>	<b>kg</b>	<b>3,454</b>	<b>3,634</b>
Unit Structural mass	kg/m <sup>2</sup>	10.28	7.83
Ballistic Coefficient	kg/m <sup>2</sup>	355	409
<b>Vehicle Entry Mass</b>	<b>kg</b>	<b>58,786</b>	<b>54,910</b>
<b>Vehicle Arrival Mass (prior to Acap)</b>	<b>kg</b>	<b>62,567</b>	<b>58,421</b>

#### D. Parametric modeling

Developing detailed vehicle point designs is labor intensive and time consuming. While it is important to understand how subsystems integrate, it is equally important to understand how the system changes with certain sets of requirements, assumptions, technologies and figures of merit. It is also important to have a consistent approach to evaluate multiple vehicle concepts and mission architectures. Therefore, the mid-L/D vehicle parametric modeling task continued in EDLAS Phase 3. The task included four activities. The first was to develop a parametric structure model to determine the sensitivity of certain design and load variables, like payload mass, vehicle scale, structural material selection and entry loads, on the overall structural mass of the vehicle. The model was generated using an automated scripting process that modified finite element models, solves load cases, then performs sizing optimization and outputs mass property information. A full description of the parametric model can be found in Ref. [17].

The second parametric modeling activity focused on evaluating alternative structures concepts like the Integrated Composite Stiffener Structure (ICoSS) and hot structures. The analysis replaced the beams and structural panels shown in Fig. 12 with the alternative structures and compared the mass saving. Additionally, various construction methods of ICoSS were also considered for comparison. While total mass savings were observed under some assumptions, further analysis is planned. Details of the study and the results are found in Ref. [17].

A third activity included advancing the system level parametric systems analysis. This activity utilized the outputs from the previous two described activities, as well as the TPS sizing effort mentioned in Section IV. By incorporating the tools and model outputs, system level trades were performed on a wide range of trajectory parameters. Parametric systems analysis and trade space exploration provides a holistic view of systems and concepts, and they provide decision makers with a better understanding of various entry system concepts and their limitations based on quantitative data. A full description of the task and results can be found in Ref. [17].

Finally, the fourth parametric modeling activity was the development of a parametric cost model. The objective of this study was to develop a cost model based on historical missions and using a commercially available code, called SEER, that includes hardware development and production costs. It develops costs based on master equipment lists. The study developed a test case with the master equipment list from the mid-L/D design presented in [19]. A validation study was performed using 12 past NASA missions. Seventy five percent of the missions fell within the 80% cost modeled by SEER. The next step was to analyze the mid-L/D point design using the model. Trades in cost per amount of payload per lander and total landed mass per surface campaign were also considered. Results indicated that mission campaigns that had to deliver the most landed mass, benefited from landers that could deliver more mass. A full description of the study and results can be found in [20].

The parametric tool capability is especially important now as we consider how the Mars architecture may change based on NASA's strategy to return to the moon. The parametric model allows for the rapid assessment of modifying the mid-L/D shape to fit on commercial launch vehicles. Likewise, the parametric modeling capability can offer insight into material selection, shape optimization, and integrated system performance that can guide the selection of the next point design to evaluate in detail.

## IV. Performance Simulations

Ideally, all model updates, including the aerodynamic interaction model described in Section II and the vehicle mass updates from Section III, are implemented in the simulation to evaluate the effect on integrated vehicle performance. However, models for both vehicles are not delivered at the same time, and so, the simulations for both vehicles do not progress at the same rate. This section presents the status of the low and mid-L/D vehicle performance results at the end of EDLAS Phase 3. The results and impact of the aerodynamic interaction model on vehicle stability and performance is presented. Other studies were performed to characterize methods to achieve direct force control of angle of attack and side slip during entry for the low-L/D vehicle [21], compare mid-L/D performance using several guidance algorithms [22], characterize RCS propellant for deorbit and entry, and evaluate navigation sensor specifications [23]. These studies are described in the references noted and therefore are not included here. Since variations in simulation fidelity exist in the results presented here, a brief description of the simulation and vehicle assumptions are provided.

### A. Effect of Aerodynamic Interactions

#### Mid-L/D

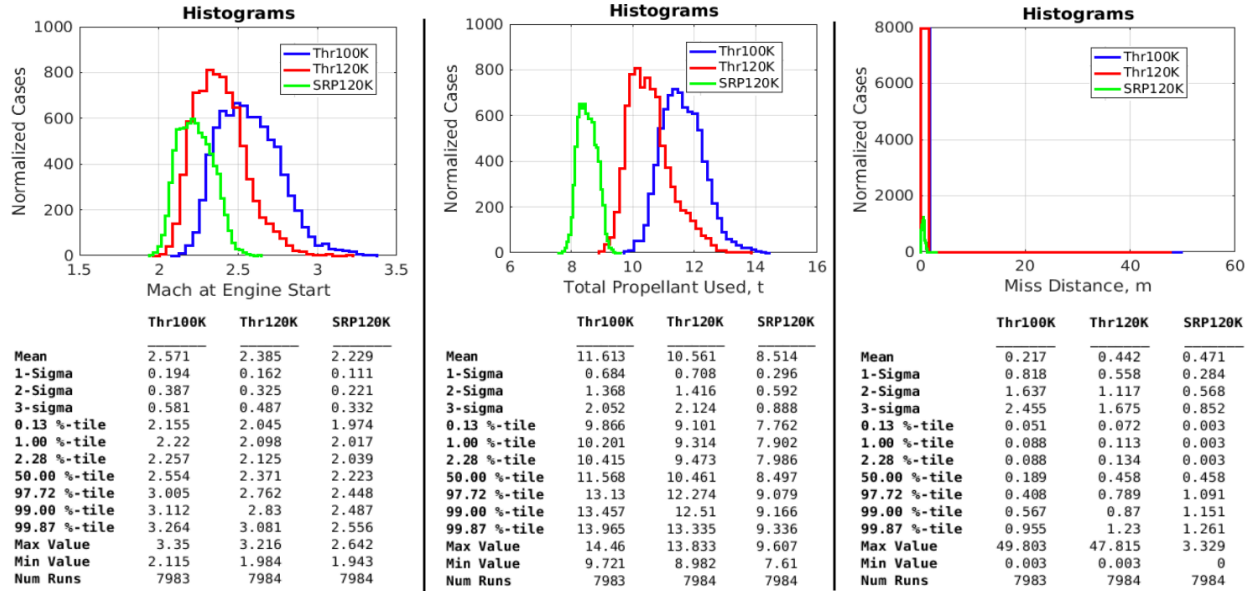
To determine the impact that aerodynamic interactions have on the mid L/D vehicle performance, the aerodynamic interaction model, presented in Section II, was implemented into the three degree-of-freedom Program to Optimize Simulated Trajectories (POST2) mid-L/D simulation. The simulation assumed a vehicle entry mass of 61.8t. The vehicle deorbited from apoapsis of a one Sol orbit (250 km x 33,800 km) and targeted a landing site of 4.98N, 24.25E and 0 km above the Mars Orbiter Laser Altimeter (MOLA) reference areoid. An instantaneous burn reduced the periapsis altitude to 10.4 km. At a sensed deceleration of 0.15 g's, the numerical predictor guidance algorithm was activated. The algorithm selected the angle of attack and sideslip to deliver the vehicle to a location at engine initiation that minimized propellant use. The guidance algorithm determined the time to start the engines. Eight engines are used for powered descent. In addition to assessing the effect of the aerodynamic interaction at engine initiation, a trade on total engine thrust was also performed. Three specific cases were considered: (1) 100 kN maximum thrust per engine with no aerodynamic interaction model (denoted as THR100K), (2) 120 kN thrust per engine with no aerodynamic interaction model (denoted as THR120K), and (3) 120 kN engines *with* the aerodynamic interaction model (denoted as SRP120K). Monte Carlo simulations of 8000 cases were run for this analysis. The Monte Carlo variables and distributions are shown in Table 6.

**Table 6. Monte Carlo dispersed parameters.**

Monte Carlo Variable	Distribution	3 $\sigma$ Maximum	3 $\sigma$ Minimum
Aerodynamics (CA, CN)	Uniform	10%	-10%
Initial Orbit Elements	Normal	Linear covariance – all diagonal terms = .01 <sup>2</sup>	
Initial Mass	Normal	1%	-1%
Deorbit Burn Bias	Normal	0.135	-0.135
Designed for $\pm .1$ deg FPA			
Atmosphere Density	Mars GRAM Model	Mars GRAM Model	Mars GRAM Model
Dusttau	Uniform	0.9	0.1

Figure 14 shows the Monte Carlo results for three key parameters including Mach number at engine initiation (left), total main engine propellant used (middle), and miss distance from the target (right side of Fig. 14). In the three Monte Carlo runs, all but 16 or 17 of the 8000 runs completed. Case 1, where each engine's maximum thrust was 100 kN (blue line – THR100K), resulted in the highest maximum Mach at engine initiation, total propellant and miss distance. Monitoring maximum propellant use, or the 99 percent-tile is important because the vehicle tank accommodation must be designed to this quantity, as opposed to the mean value, which effects on the tank sizes and packaging. Depending on the available lander packaging volume, propellant mass and volume growth can translate into higher deck heights, higher center of gravity, landing systems and vehicle stability. Additionally, the case resulted in the largest dispersion (between the 1 and 99 percent-tile) in Mach number and total propellant used. To compare only the effect of increasing total engine thrust from 100 to 120 kN, case 2 (THR120), the blue line is compared to the red. An advantage of more thrust is lower propellant use, but it does not reduce the 1 to 99 percentile dispersion range significantly. In fact, the landed miss distance range is slightly larger for this case. However, when the aerodynamic interaction model is included with 120kN engines (shown in green- SRP120K), the result significantly

reduces the 99 percent-tile Mach number at engine initiation from 3.1 to 2.5. Likewise, the 99 % propellant use drops from 12.51t to 9.2 t.



**Fig. 14 Mid-L/D 3-DOF simulation statistics for Mach number at engine initiation (left), total propellant (middle), and landed miss distance (right).**

The mid-L/D aerodynamic interaction model was designed assuming the vehicle does its pitch over maneuver before starting the engines (flying at 90 deg angle of attack) when in reality it may be somewhere between 55 and 90 deg, in which case the aero interaction effect would be less and result in a less significant propellant mass savings. As the mid L/D vehicle fidelity increases, additional work is needed to characterize the aerodynamic interactions effects for changing angles of attack as well as differentially throttled engines.

#### Low-L/D

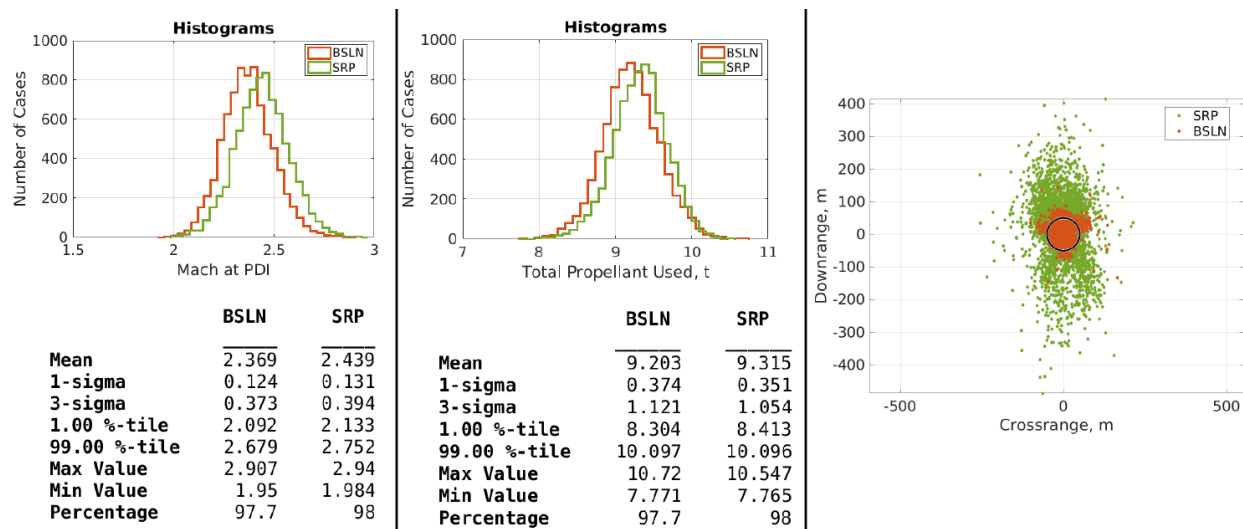
The EDL concept of operations for the low-L/D vehicle is similar to the mid-L/D vehicle concept of operations described in the previous section. The low-L/D vehicle is assumed to have a 16.4 m diameter, an entry mass of 49 t, and use eight 100 kN engines in the Doublet-A configuration (See Fig. 2). Due to the lower entry mass compared to the mid-L/D, 120 kN engines were not considered as part of this analysis. A similar numerical predictor corrector guidance approach is used. The primary difference in the analysis is that the low-L/D study used a POST2 six degree-of-freedom simulation (6-DOF). Therefore, higher fidelity Monte Carlo parameters were included in the analysis. They are listed in Table 7.

**Table 7. Low-L/D 6-DOF Monte Carlo dispersions.**

Parameter	Dispersion
State covariance	Inclination: 0.01° 1σ Long. Asn. Nd.: 0.01° 1σ Alt. Per.: 20 m 1σ Alt. Apo.: 20 m 1σ True Anomaly: 0.01° 1σ Arg. Per.: 0.01° 1σ
SRP Interference	Mach dependent, 2.78-0.8 CA: ±0.27-0.08 3σ, normal CN: ±0.03-0.04 3σ, normal CY: ±0.03-0.04 3σ, normal CMX: ±4.85e-3 to 0.00 3σ, normal CMY: ±0.02-0.02 3σ, normal CMZ: ±0.01-0.02 3σ, normal
CG	±5 cm 3σ, normal

Inertias	±5% 3σ, normal
Mass	±500 kg 3σ, normal
Deorbit burn execution error	±13.5 cm/s 3σ, normal
Aerodynamics	IRVE-3 derived uncert. and MSL
Opacity	0.1:0.9, uniform
Density and winds	Mars-GRAM uncertainties
Aerodynamics	IRVE-3 derived uncert. and MSL
Peak engine thrust	±1% 3σ, normal
Peak engine Isp	±1% 3σ, normal
Engine start lag	0.0:0.2 s, uniform
Engine startup rate	±1% 3σ, normal
Engine main phase rate	±1% 3σ, normal
Engine shutdown rate	±1% 3σ, normal

Results of the low-L/D 6DOF analyses are shown with statistics in Fig.15 for the same parameters considered in the mid-L/D analysis. However, the impact of the aerodynamic interaction model on the low-L/D vehicle is less prominent. In fact, the 99 percentile Mach number at engine initiation is slightly higher than the baseline case (2.74 compared to 2.67 in the baseline) and the propellant use is nearly identical. However, it is noted that the landing dispersions at touchdown are less using the aerodynamic interaction model. See the right side of Fig. 15.



**Fig. 15 Low-L/D 6-DOF simulation statistics for Mach number at engine initiation (left), total propellant (middle), and landed miss distance latitude and longitude (right).**

The reason the aerodynamic interaction model had a more prominent effect on the mid-L/D compared to the low-L/D vehicle was because the mid-L/D engine integration (outboard and canted outward) into the vehicle permits substantial aerodynamic surface area to remain unobstructed by the exhaust plumes during the supersonic portion of descent. The additional aerodynamic drag during powered descent is a mass-free contribution to the deceleration of the vehicle, reducing the amount of propellant required to land. Ultimately, minimizing the aerodynamics interference effects during powered flight will result in the lowest risk and cost of flight implementation. While that will be difficult for the mid-L/D vehicle to reduce the effect, the low-L/D vehicle potentially has more options. The low-L/D also has significant aerodynamic surface area, but the engines are integrated further inboard on the vehicle. Planned wind tunnel tests evaluating various engine configurations and cant angles outlined in Section II.C will inform the vehicle design that minimizes the uncertainty of the effects. However, other system impacts remain to be considered like vehicle stability, controllability and plume surface interactions.

## V. Technology Investment Recommendations

The EDLAS Phase 3 effort was able to make strides to resolve the knowledge gaps for aerodynamic interactions with the engine plumes at engine initiation using CFD. Wind tunnel tests planned for 2020 will help to validate the CFD. However, the effort highlighted still other areas for future work. One area of critical importance is characterizing surface plume interactions. The high fidelity trajectory simulations continue to improve knowledge of the flight environment just prior to landing but additional work to design landing gear robust to the landing environment is still needed. Likewise, onboard computing to handle the guidance algorithms and sensor image processing required to achieve precision landing is still needed. Additional options for guidance algorithms are sought to improve delivery accuracy of both the entry and descent flight phase. Navigation sensor vehicle accommodation and operation remain a concern and require validation to achieve precision landing requirements. Studies are underway to consider various ground and flight tests that could drive down risk and validate models in all these areas. Additionally, new robotic and human scale missions at the moon offer opportunities to test either individual technologies like a navigation sensor or guidance algorithm or validating codes for surface plume interaction. Likewise, the lunar missions could offer system level or integrated guidance, navigation and control test beds for Mars EDL algorithms and sensors. Despite the difference in local gravitation and lack of an atmosphere, the moon offers many opportunities to mature Mars EDL technologies. Work continue to identify opportunities to incorporate Mars EDL related technologies on near term ground, flight and lunar missions.

## VI. Conclusion

Over the past three years, EDLAS has been evaluating candidate technologies to deliver human scale vehicles to the surface of Mars. Phase 3 of the study focused the design space on two entry vehicles and extended technology assessment to various subsystems. This paper summarized some of the analysis used to characterize aero interaction characterization during the powered flight phase, update the mid-L/D design, and improve performance analysis of both vehicles. This paper serves only as a broad system level summary of the overall effort and provides an extensive list of references that describe individual elements of the study in greater detail. Work continues to improve the fidelity of each vehicle design. Aspects of future work include updating the hypersonic aerodynamic and aerothermodynamic databases, characterizing the surface plume interactions and landing design. Likewise, results of the wind tunnel campaign will be incorporated into the initial aerodynamic interaction models. Ultimately the results of new activities to characterize surface plume interactions will be incorporated into landing and sensor performance evaluations. While many technical challenges remain, a primary future effort of this study is to move beyond modeling and simulation and onto identifying and developing ground and flight test opportunities that will take these vehicles off of paper and into flight.

## Acknowledgments

The authors would like to acknowledge the Science Technology Mission Directorate (STMD) and the Human Exploration and Operations Mission Directorate (HEOMD) for their continued support of this and other studies that continue to challenge our EDL paradigms. The authors would like to recognize Tara Polsgrove and all the members of the EDLAS Team. They come from many NASA centers including, Ames Research Center, Langley Research Center, Johnson Spaceflight Center and Marshall Space Flight Center, as well as, external contractors and those in academia. While they are too numerous to list here, the work summarized in this paper is based on their collective contributions.

## References

- [1] Cianciolo, A. D. and Polsgrove, T. T., "Human Mars Entry, Descent and Landing Architecture Study Overview," AIAA Paper 2016-5494, Sept. 2016.
- [2] Drake, B. G., editor, "Human Exploration of Mars Design Reference Architecture 5.0," s.l. : NASA SP-2009-566, 2009.
- [3] Craig, Douglas A., Herrmann, Nicole B., and Troutman, Patrick A. "The Evolvable Mars Campaign – Study Status," IEEE Aerospace Conference, Big Sky, MT, March 7-14, 2015.
- [4] Cianciolo, A. D. and Polsgrove, T. T., "Human Mars Entry, Descent and Landing Architecture Study: Phase 2 Summary," AIAA 2018-5190.
- [5] Korzun, A., Canabal, F., Tang, C., Childs, R., Van Norman, J., Tynis, J., Bibb, K. "Powered Descent Aerodynamics for Low and Mid Lift-to-Drag Human Mars Entry, Descent and Landing Vehicles." AIAA SciTech 2020 Abstract Accepted.
- [6] Biedron, R. T., Derlaga, J. M., Gnoffo, P. A., Hammond, D. P., Jones, W. T., Kleb, B., Lee-Rausch, E. M., Nielsen, E. J., Park, M. A., Rumsey, C. L., Thomas, J. L., and Wood, W. A. "Fun3D Manual: 12.7," NASA TM 2015-218761, May 2015.
- [7] Luke, E., George, T. "LocI: A Rule-Based Framework for Parallel Multidisciplinary Simulation Synthesis." Journal of Functional Programming. Vol 15, pp. 477-502 2005.
- [8] Wright, M. W., White, T., and Mangini, N., "Data Parallel Line Relaxation (DPLR) Code User Manual Acadia Version 4.01.1," NASA TM-2009-215388, Oct. 2009.
- [9] Nichols, R., and Buning, P., User's Manual for OVERFLOW 2.1t, University of Alabama, Birmingham, AL, Aug. 2008.
- [10] Schauerhamer, D. G., Zarchi, K. A., Kleb, W. L., Carlson J.-R., Edquist, K. T. "Supersonic Retropropulsion Computational-Fluid Dynamics Validation with Langley 4x4 Foot Test Data" Journal of Spacecraft and Rockets Vol 51 pp 693-714 (2014).
- [11] Schauerhamer, D. G., Zarchi, K. A., Kleb, W. L., Edquist, K. T. "Supersonic Retropropulsion Computational-Fluid Dynamics Validation with Ames 9x7 Foot Test Data" Journal of Spacecraft and Rockets Vol 51 pp 735-749 (2014).
- [12] Korzun, A., Nielsen, Walden, Jones, Carlson, Moran, Henze, Sandstrom. "Effects of Spatial Resolution on Retropropulsion Aerodynamics in an Atmosphere Environment." AIAA SciTech 2020 Abstract Accepted.
- [13] Edquist, K. "Model Design and Pre-Test CFD Analysis for a Supersonic Retropropulsion Wind Tunnel Test." AIAA SciTech 2020 Abstract Accepted.
- [14] Cerimele, C. J., Robertson, E. A., Sostaric, R.R., (editor), Garcia, J. A. "A Rigid, Mid-Lift-to-Drag Ratio Approach to Human Mars Entry, Descent, and Landing", AIAA SciTech 2017, Grapevine, TX, Jan. 2017.
- [15] Polsgrove, T. T., Percy, T. K., Garcia, J., Cianciolo, A. D. Samareh, J., Lugo, R., Robertson, E., Cerimele, C., Sostaric, R., and Garcia, J., "Human Mars Entry, Descent and Landing Architecture Study: Rigid Decelerators," AIAA 2018-5192.
- [16] Calderon, D. T., Sostaric, R. R., Garcia, J. A., Bowles, J. V., Gaytan, C., Newton, H., Amar, J., and Wiens, Z. "Structural Mass Optimization with Manifest Packaging, and Outer Mold Line Updates of a Rigid Mid Lift-to-Drag Mars Entry Lander Entry Vehicle." AIAA SciTech 2020 Abstract Accepted.



- [17] Samareh, J. A., Behrend, M. P., Poteet, C. C., Komar, D. R., Theisinger, J. E., Lugo, R. A., and Bowles, J. V., "Parametric Systems Analysis of a Mid-Lift/Drag Entry System for Human Mars Mission," AIAA SciTech 2020 Abstract Accepted.
- [18] Garcia, J.A., Brown, J. L., Kinney D. J., Bowles, J. V., Huynh L.C., Jiang X.J., Lau E., Dupzyk, I.C., "Co-Optimization of Mid Lift to Drag Vehicle Concepts for Mars Atmospheric Entry," 10th AIAA/ASME Thermophysics Conference, 2010.
- [19] Brown, J.L., Garcia, J.A., Kinney, D.J., Bowles, J.V., Mansour, N.N., U.S. Patent entitled "Co-Optimization of Blunt Body Shapes for Moving Vehicles" issued in 2014, Patent No.: US8725470.
- [20] Friz, P. D., "Parametric Cost Estimates of Four 20 Ton Payload Mars EDL Vehicle Concepts," Abstract Accepted SciTech2020 Abstract Accepted.
- [21] Cianciolo, A. D., Korzun, A., Lugo, R. A., Slagel, A., Queen, E., Dillman, R., Powell, R. "Low Lift-to-Drag Morphing Shape Design." AIAA SciTech 2020 Abstract Accepted.
- [22] Johnson, B., Sostaric, R., Lu, P. "Mid Lift-to-Drag Rigid Vehicle 6-DoF Performance for Human Mars Entry, Descent, and Landing." AIAA SciTech 2020 Abstract Accepted.
- [23] Cianciolo, A. D., Lugo, R. A., Dutta, D., Williams, A., Chen, P. "A Simulation Framework for Precision Landing and Hazard Avoidance Technology Assessments." AIAA SciTech 2020 Abstract Accepted.